Materials Research Bulletin 152 (2022) 111849

Contents lists available at ScienceDirect

Materials Research Bulletin

journal homepage: www.elsevier.com/locate/matresbu

Efficient Ni and Fe doping process in ZnO with enhanced photocatalytic activity: A theoretical and experimental investigation

Samantha Custódio Silva Lemos [a,b], Thaís Karine de Lima Rezende [a], Marcelo Assis [b,c], Fernanda da Costa Romeiro [a,d], Diego Alves Peixoto [a], Eduardo de Oliveira Gomes [c], Gabriel Marques Jacobsen [e], Marcio Daldin Teodoro [e], Lourdes Gracia [c], Jefferson Luis Ferrari [a], Elson Longo [b], Juan Andrés [c,*], Renata Cristina de Lima [a,*]

[a] Instituto de Química, Universidade Federal de Uberlândia, Uberlândia, MG 38400-902, Brazil
[b] CDMF-Centro de Desenvolvimento de Materiais Funcionais, Departamento de Química, Universidade Federal de São Carlos, São Carlos, SP 13565-905, Brazil
[c] Departament de Química Física i Analítica, Universitat Jaume I, Castellon 12071, Spain
[d] Instituto de Química, Universidade Estadual Paulista, Araraquara, SP 14800-060, Brazil
[e] Departamento de Física, Universidade Federal de São Carlos, São Carlos, SP 13565-905, Brazil

ARTICLE INFO

Keywords:
ZnO
Transition metals
Microwave-assisted hydrothermal
Photocatalysis
Optical properties
DFT calculations

ABSTRACT

$Zn_{1-x}Ni_xO$ and $Zn_{1-x}Fe_xO$ structures were synthesized by the microwave-assisted hydrothermal method. The best photocatalytic degradation of rhodamine B (RhB) and 4-nitrophenol (4-NP) were achieved by the $Zn_{0.96}Ni_{0.04}O$ and $Zn_{0.99}Fe_{0.01}O$. The specificity of each dopant showed significance in the positions of the impurity energy levels, which ended up influencing the electron-hole separation and transport, as demonstrated by the photoluminescence emissions. The morphological analysis revealed that besides inhibiting the growth of particles, the incorporation of dopant ions into the ZnO lattice triggered a nucleation process, consequently changing their morphology. Density functional theory (DFT) calculations showed that the Fe^{3+} 3d orbitals generate energy levels below the conduction band (CB) while for Ni^{2+}, the levels were found to be spread in a broad energy range above the valence band (VB). The synergistic effect of band gaps alteration, inhibition of electron-hole pair recombination and appearance of new trapping energy sites justifies the superior photocatalytic activity.

1. Introduction

Organic dyes and their effluents have become one of the major sources of water pollution because of extensive consumption of chemicals by the textile industries [1]. As they are harmful to the environment, hazardous to human health and not easily degradable [2,3], an ecofriendly and energy-saving method for their degradation/elimination is strongly desired to treat the industrial wastewater [4,5]. Photocatalysis is known as a cheap and environmentally-friendly technology that has drawn much attention since proposed by Fujishima and Honda [6,7]. In this way, the development of efficient, stable, and low-cost semiconducting photocatalysts play a key role in highly functional and economically viable photocatalysis. N-type semiconducting photocatalysts, including SnO_2, [8] TiO_2, [9,10] ZnO, [3,11] and In_2O_3 [12] were found suitable for photocatalytic process owing to their non-toxicity, wide bandgap, and high photosensitivity and photo-stability.

Zinc oxide (ZnO) is an n-type binary semiconductor with a hexagonal wurtzite structure that has partially polar characteristics [13]. This material presents intrinsic defects, such as zinc interstitial (Z_i) and oxygen vacancy (V_o) in its crystal structure and also a direct bandgap value of 3.37 eV. In addition, its large exciton binding energy of ~ 60 meV has demonstrated high quantum efficiency and photocatalytic activity. [14,15] However, like most photocatalysts, it is only active in the UV region and presents a high recombination rate of the photogenerated electron-hole (e^-/h^+) pairs, which ends up limiting its utilization [16].

The incorporation of dopants significantly changes the band gap of ZnO as a result of the appearance of intermediate energy levels within the forbidden region [17]. Additionally, this process can affect the crystalline structure, surface area, crystallite size and morphology of this oxide, as well as its physical and chemical properties [18–23]. In order to increase its technological applications, such characteristics can be tuned by choosing appropriate dopants and their concentration [24–26].

* Corresponding authors.
E-mail addresses: andres@qfa.uji.es (J. Andrés), rclima@ufu.br (R.C. de Lima).

https://doi.org/10.1016/j.materresbull.2022.111849
Received 27 October 2021; Received in revised form 5 April 2022; Accepted 6 April 2022
Available online 9 April 2022

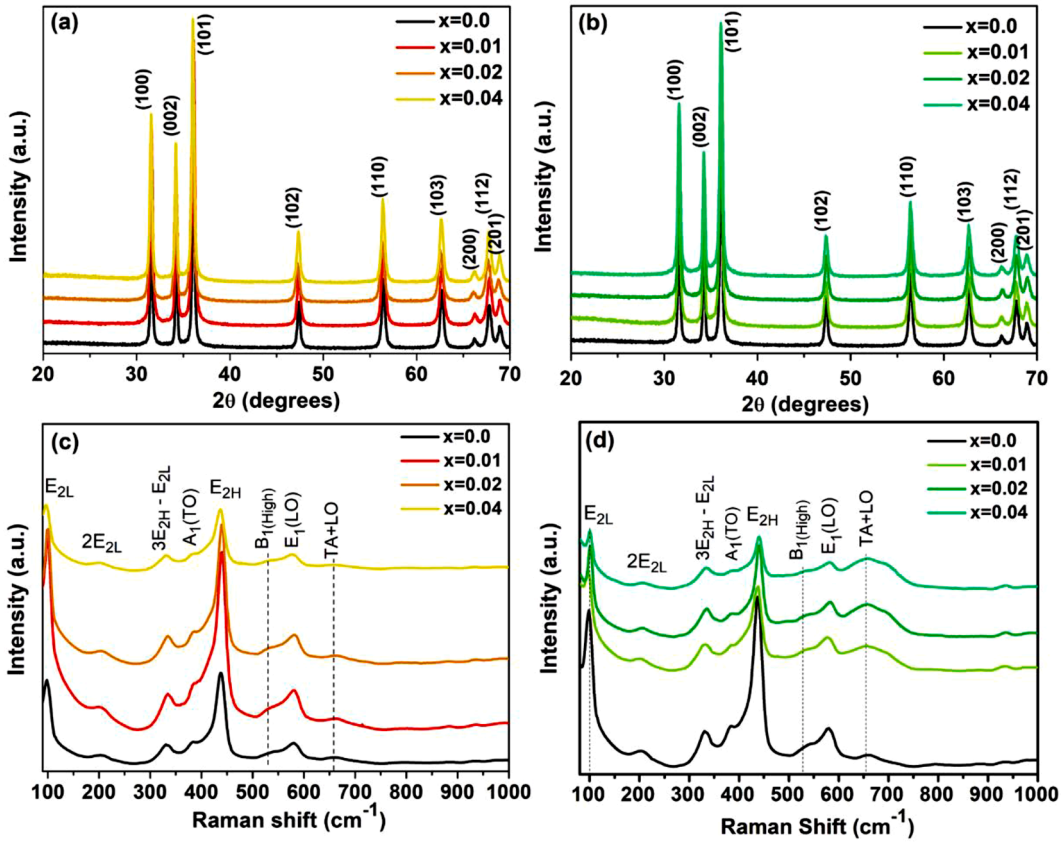

Fig. 1. XRD and Raman spectra results of (a-c) $Zn_{1-x}Ni_xO$ and (b-d) $Zn_{1-x}Fe_xO$ (x=0.01; 0.02 and 0.04 mol) samples obtained by the MAH method, x= mol of Ni^{2+} or Fe^{3+}.

Recently, the incorporation of metallic ions such as Co^{2+} [27,28], Ni^{2+} [29,30], Fe^{3+} [30] and Sn^{4+} [20], into the ZnO structure to tune its properties, including its photocatalytic visible-light response, has also been investigated. Ji et al. [20] showed that the degradation rate of methylene blue by $Sn_{0.05}ZnO$ reached 99.61% after 120 min of illumination, which was approximately 2.2 times higher than undoped ZnO. Neena et al. [31] synthesized g-C_3N_4-coupled Fe-doped ZnO micro-flowers and observed enhanced photocatalytic performance in the photo-degradation of the 2,4-dichlorophenol pollutant as a result of simultaneous Fe doping and coupling with g-C_3N_4. According to Beura and Thangadurai [2] the best photocatalytic activity was achieved with 1 wt% of Sn doping into the graphene/ZnO matrix. This enhancement was associated with optimum doping content, decreased band gap (2.87 eV), sustaining lifetime (15.72 ns), reduced recombination of charge carriers and increased generation of hydroxyl radicals, $^{\bullet}OH$, during photocatalysis. The photocatalytic photodegradation of degradation of rhodamine B (RhB) using $Ni_xCo_xZn_{1-2x}O$ nanoparticles studied by Pascariu et al. [28] evidenced the sensitivity of the catalyst response to the concentration of dopants.

An analysis of the scientific literature renders that different morphologies of ZnO have been reported, including: nanowires, nanorods, nanorings, nanotubes, nanospheres, nanoflowers and nano-needles. It is known that such morphologies are extremely important to enable the improvement of a given technological application [32–35]. Hui et al. [36] discussed the effect of Fe doping on the band gap and morphology of ZnO. According to the authors, the 5% Fe-doped ZnO sample showed the highest RhB degradation efficiency (~97.70%). On the other hand, Byzynski et al. [37] established that the crystal face exposure strongly influences the properties of N-doped ZnO crystals, whose particles with oriented nanorods were found to inhibit the recombination of carriers better than N-doped ZnO nanostructures, besides presenting enhanced photocatalytic activity. It can then be concluded that the decrease of specific surface area or band gap by the doping process can influence the potential applications of metal-doped ZnO and that the morphology plays an important role in this process due to the direct influence of the dopants on its electronic and physicochemical properties. However, consistent studies connecting the morphology with the photocatalytic performance are still needed.

In this study we report the facile synthesis of ZnO, $Zn_{1-x}Ni_xO$ and $Zn_{1-x}Fe_xO$ (x=0.01; 0.02 and 0.04 mol) samples via the microwave-assisted hydrothermal (MAH) method for the photocatalytic degradation of rhodamine B (RhB) and 4-nitrophenol (4-NP). The doping process with Ni^{2+} and Fe^{3+} cations affected the photoluminescence emissions, size and morphology of ZnO particles. Higher concentration of Ni^{2+} favored the photodegradation process, while the photocatalytic efficiency of $Zn_{1-x}Fe_xO$ was improved with the decrease of Fe^{3+} concentration. To complement and rationalize the experimental results, first-principles calculations were performed at the density functional theory (DFT) level to describe the electronic properties, explore the ferromagnetic and antiferromagnetic ordering and elucidate the distinct effects of 3d states of the dopants within the band gap of the ZnO system. The specificity of each dopant shows significance in changing the forbidden bandwidth and the positions of the impurity energy levels, which ends up influencing the formation, transport and recombination of photocatalytic carriers.

2. Experimental

2.1. Samples preparation

The ZnO sample was obtained from the addition of 4.9×10^{-3} mol of $Zn(CH_3COO)_2.2H_2O$ in 40.0 mL of distilled water under constant

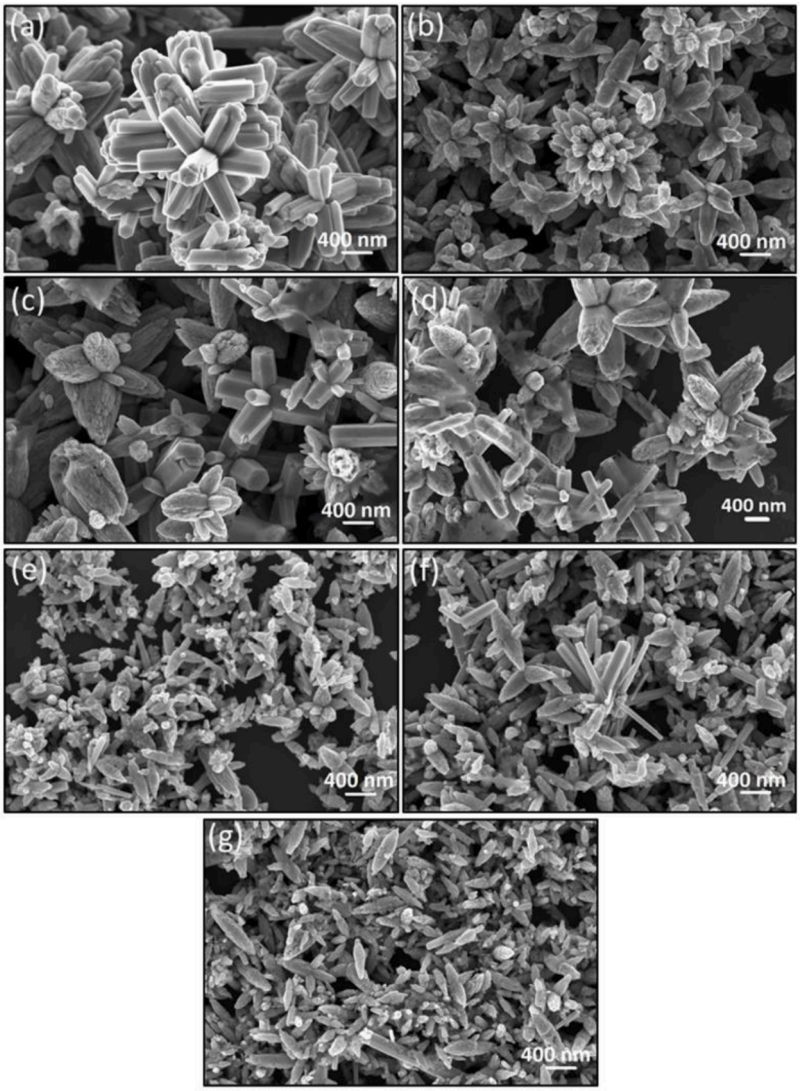

Fig. 2. FE-SEM images of $Zn_{1-x}Ni_xO$ and $Zn_{1-x}Fe_xO$ samples (a) x=0.0 (b) x=0.01 mol of Ni^{2+} (c) x=0.02 mol of Ni^{2+} (d) x=0.04 mol of Ni^{2+} (e) x=0.01 mol of Fe^{3+} (f) x=0.02 mol of Fe^{3+} and (g) x=0.04 mol of Fe^{3+}.

stirring. Concentrated ammonium hydroxide was added until pH = 9. The same procedure was employed to obtain $Zn_{1-x}Ni_xO$ and $Zn_{1-x}Fe_xO$ samples (x = 0.01; 0.02 and 0.04 mol of Ni^{2+} and Fe^{3+} ions), plus the addition of stoichiometry concentrations of $Ni(NO_3)_2.6H_2O$ and $Fe(NO_3)_3.9H_2O$ precursors. The solutions were transferred into a Teflon autoclave, and then sealed and annealed under hydrothermal conditions at 120°C and a heating rate of 5 °C min^{-1}. Upon reaching the temperature, the solution was kept under heating for 1 minute. The products obtained were centrifuged, washed with water and ethanol and dried at 70 °C for 2 h.

2.2. Materials characterization

The crystallographic structures of undoped ZnO, $Zn_{1-x}Ni_xO$ and $Zn_{1-x}Fe_xO$ powders were characterized in a Rigaku X-ray diffractometer (model DMax2500PC) operating at 40 kV and 150 mA using Cu-Kα radiation (λ = 1.5406 Å). Field emission scanning electron microscopy (FE-SEM) and transmission electron microscopy (TEM) were performed on FE-SEM JEOL model 7500F and Jem-2100 LaB6 (Jeol) microscopes, respectively. Raman measurements were carried out on an Ocean Optics spectrometer at λ = 785 nm. The UV-vis spectra of the materials were obtained using a Cary spectrophotometer (model 5G) in the range between 200 and 800 nm. Photoluminescence (PL) measurements were performed at room temperature by using a 355 nm laser (Cobolt/Zouk) as excitation source, focused on a 200 μm spot at a constant power of 5 mW

2.3. Photocatalytic studies

The photodegradation tests were performed with RhB (RhB, Synth, 99.9%) solution (1×10^{-5}M) and 4-NP (Aldrich, >99%) solution (10 ppm). 50.0 mg of each sample was added to the pollutant solution (50.0 mL). These dispersions were placed in the ultrasound system for medium dispersion and then taken to the dark for 30 min for adsorptive equilibrium. Afterwards, a system containing ultraviolet-visible lamps (6x Philips TLD-15W) was switched on, and aliquots were removed at predetermined times. The aliquots were analyzed by absorption spectrophotometry in the UV-Visible region. For the photodegradative stability tests, the same process was carried out 4 more times using the same materials. Equimolar amounts of L-ascorbic acid (AA, Aldrich, 99%), tert-butyl alcohol (TBA, Aldrich, 99.5%), ammonium oxalate (AO, Aldrich, 99%) and silver nitrate (SN, Cennabras, 99.8%) were added for the scavenger tests with RhB.

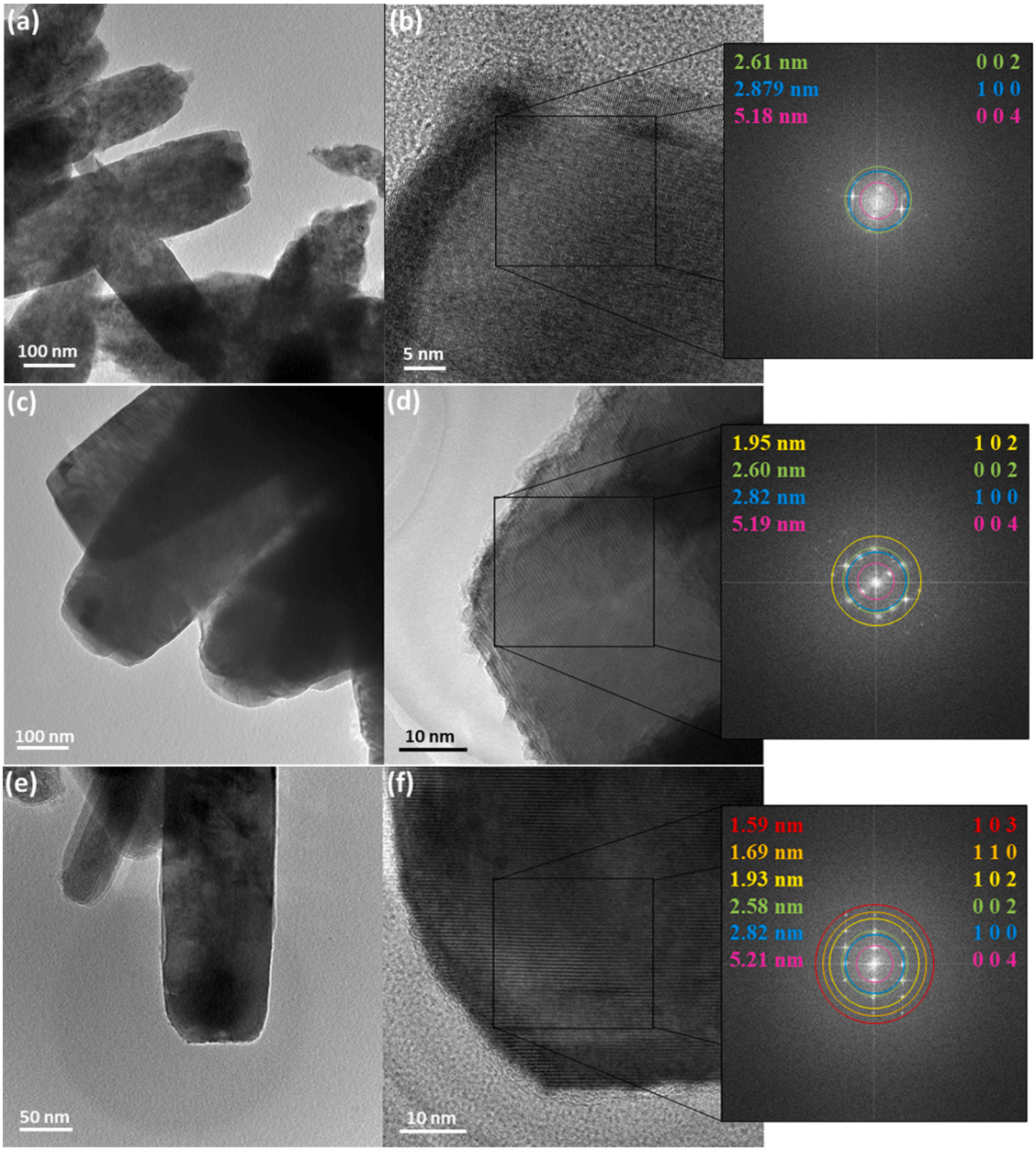

Fig. 3. TEM and HRTEM images of (a-b) undoped ZnO (c-d) $Zn_{0.96}Ni_{0.04}O$ and (e-f) $Zn_{0.99}Fe_{0.01}O$ samples. SAED patterns are on the right side.

2.4. Computational methods

First principles calculations within the periodic DFT framework, using the hybrid Perdew–Burke-Ernzerhof exchange-correlation functional (PBE0) [38] were performed with CRYSTAL17 software [39] to characterize the undoped ZnO and Fe^{3+} and Ni^{2+}-doped ZnO systems. All the systems were investigated within the Unrestricted Hartree–Fock (UHF) approximation to allow a description of the spin polarization as a result of the unpaired d electrons of the dopant ions. All-electron basis sets were used to describe the O [40], Zn [41], Fe [42] and Ni [43] atomic centers. Regarding the density matrix diagonalization, the reciprocal space net was described by a shrinking factor of 4, corresponding to the Monkhorst-Pack scheme. The accuracy of the evaluation of the Coulomb and exchange series was controlled by five thresholds, whose adopted values were 10^{-8}, 10^{-8}, 10^{-8}, 10^{-8}, and 10^{-16}. In order to reflect low Fe and Ni concentrations, a supercell expansion corresponding to $2 \times 2 \times 2$ containing 32 atoms was calculated to simulate the ZnO and the ferromagnetic (FM) Fe^{3+}- and Ni^{2+}-doped ZnO systems. This arrangement resulted in a structure with 6.50% substitution of Zn^{2+} ions by Ni^{2+} cations and by Fe^{3+} cations (in the case of Fe^{3+} doping with formation of a Zn^{2+} vacancy in the structure). Also considering the influence of anti-ferromagnetism (AFM), an appropriate supercell with twice of the volume of the supercell used for the FM systems was built to perform the calculations in order to investigate the contribution of the different dopant spin arrangements to the electronic properties of ZnO.

3. Results and discussion

3.1. Structural analysis

X-ray diffraction (XRD) patterns of undoped ZnO, $Zn_{1-x}Ni_xO$ and $Zn_{1-x}Fe_xO$ powders are shown in Fig. 1a,b. All Bragg peaks are indexed to a wurtzite-type structure of zinc oxide (JCPDS 36-1451, space group $P6_3mc$), indicating the incorporation of Ni^{2+} and Fe^{3+} ions into the ZnO lattice under microwave hydrothermal conditions. The crystallite size (D) determined from the XRD line broadening measurements from

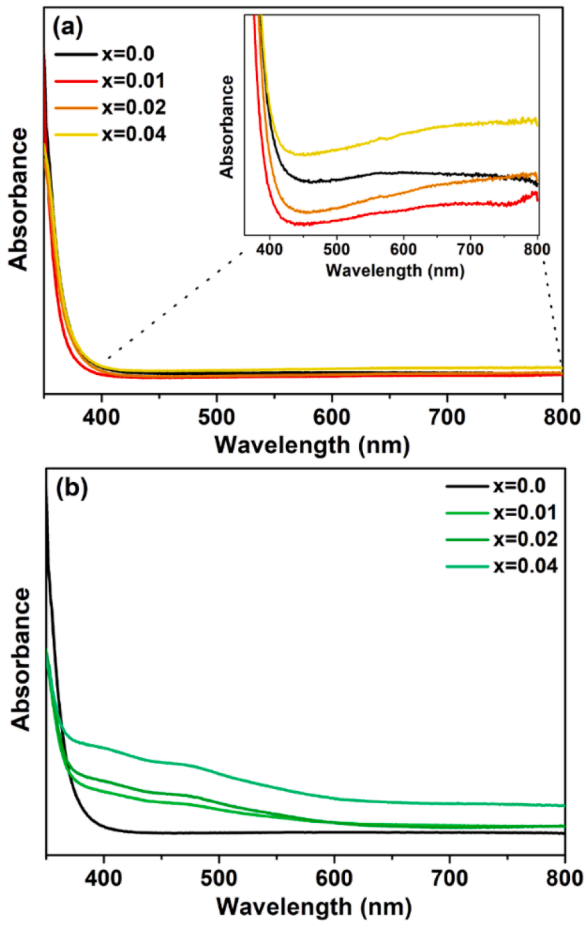

Fig. 4. Optical absorbance spectra of (a) $Zn_{1-x}Ni_xO$ and (b) $Zn_{1-x}Fe_xO$ (x=0.01; 0.02 and 0.04 mol) samples obtained by the MAH method, x= mol of Ni^{2+} or Fe^{3+}.

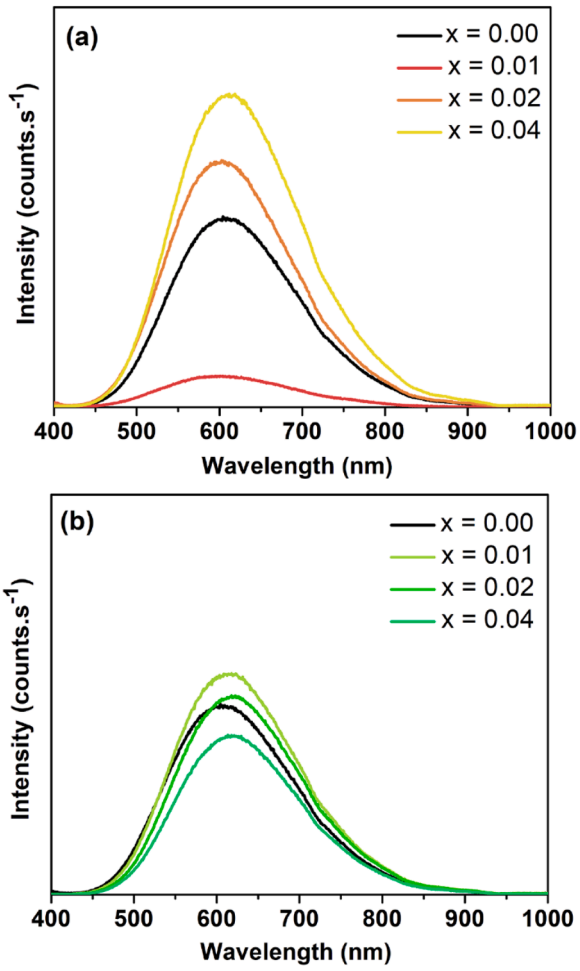

Fig. 5. PL spectra of (a) $Zn_{1-x}Ni_xO$ and (b) $Zn_{1-x}Fe_xO$ (x=0.01; 0.02 and 0.04 mol) samples at room temperature (λ_{exc}= 355 nm) prepared by the MAH method; x= mol of Ni^{2+} or Fe^{3+}.

Debye Scherrer equation are presented in supporting information, Table S1. It can be observed that the doped samples undergo a decrease in crystallite size in comparison with the undoped ZnO.

The Raman spectra of the ZnO, $Zn_{1-x}Ni_xO$ and $Zn_{1-x}Fe_xO$ samples are shown in Fig. 1c,d, where it can be seen that all samples exhibit a peak around 437 cm^{-1} related to the E_2 (high) mode corresponding to the wurtzite structure [14,27]. The peaks at 101, 204, 334 and 385 cm^{-1} are ascribed to E_{2L}, $2E_{2L}$, $3E_{2H}$-E_{2L} and A_1(TO) phonon modes, respectively, which are characteristic of zinc oxide [44,45]. The additional peak around 528 cm^{-1} corresponds to $B_{1(high)}$ [46], whereas those around 581 and 655 cm^{-1} refer to the E_1(LO) and (TA + LO) modes in ZnO, respectively [27,45]. The E_{2H} modes become weak with the incorporation of Ni^{2+} and Fe^{3+} ions into the host matrix, which can be attributed to the higher structural disorder induced by doping [47]. No additional Raman modes due to secondary phases involving metallic ions can be observed, which corroborates the XRD results.

3.2. FE-SEM and TEM analysis

FE-SEM images of the ZnO, $Zn_{1-x}Ni_xO$ and $Zn_{1-x}Fe_xO$ samples are displayed in Fig. 2. It can be noted that the ZnO sample has a flower-like assembled morphology of about 1.6 μm in width, composed of nanorods petals (Fig. 2a). The Ni^{2+}-doped ZnO samples, on the other hand, exhibit a non-uniform flower-like morphology formed by nanorods and elongated petal structures, as shown in Fig. 2b–d. However, with the increase in the amount of Fe^{3+} ions, the morphologies drastically change, and the formation of elongated and dispersed petals start to appear, as observed in Fig. 2e–g.

Results of average particle size distributions and average particle size length and width from microscopy images are shown in supporting information, Fig. S1 and Table S2. It can be seen that the ZnO rods present average length and width of ~781.4 and 283.2 nm, respectively. For all doped samples, there is a decrease in the particle size, being 606.1 nm and 280.6 nm the calculated value of length and width for sample $Zn_{0.96}Ni_{0.04}O$, respectively, and around 256.5 nm and 126.4 nm for sample $Zn_{0.99}Fe_{0.01}O$, respectively. It is known that the addition of impurities may influence the size and morphology of ZnO due to their effective participation on the particle nucleation and growth, in which many factors contribute to the crystal growth process of nanostructures [48]. The particle size distributions can corroborate the crystallite size presented in Table S1 (supporting information), where it is possible to note that the flower-like morphologies of the ZnO structures present higher crystallite size than the doped samples. Al-Gaashani et al. [49] showed in their study that ZnO nanoparticles presented smaller crystallite size than nanoflowers and nanorods, following the order: nanorods > nanoflowers > nanoparticles. These observations are in agreement with the results reported herein, which demonstrated that the adding of a doping amount in the ZnO lattice changes and decreases the length and width of the petals of the flower-like assembled ZnO morphology.

In the beginning of ZnO formation process, ammonium hydroxide was added to zinc acetate dispersion, leading to the formation of amorphous seed nuclei. During microwave heating, clusters are formed by collision and atoms are rearranged, followed by nucleation of

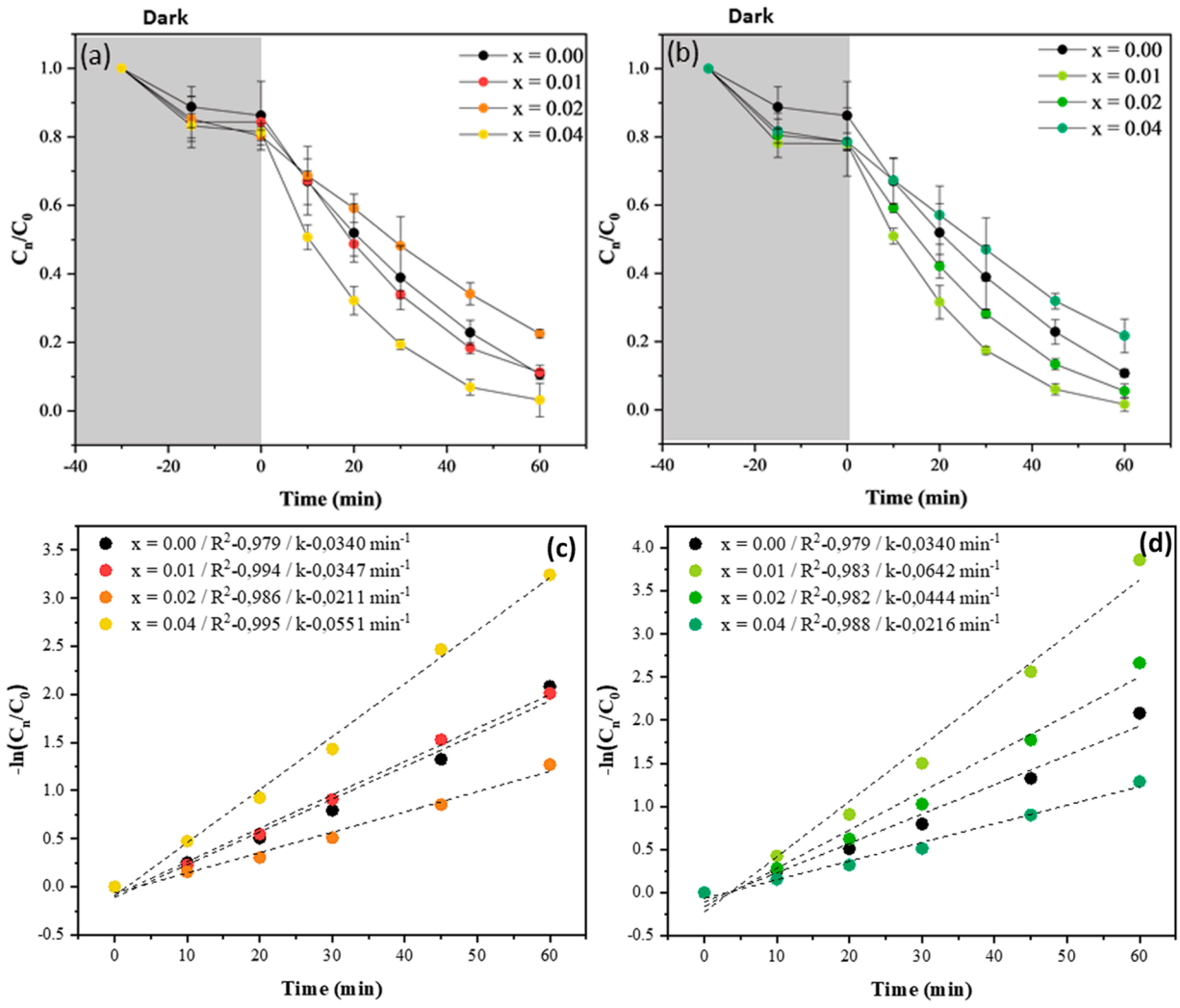

Fig. 6. Curves of photodegradation of RhB using (a) $Zn_{1-x}Ni_xO$ (b) $Zn_{1-x}Fe_xO$ (x=0.01; 0.02 and 0.04 mol) photocatalysts under UV-vis irradiation. Rate constant, k, (-ln C/C_0) as a function of irradiation time using (c) $Zn_{1-x}Ni_xO$ (d) $Zn_{1-x}Fe_xO$ photocatalysts; x= mol of Ni^{2+} or Fe^{3+}.

nanoparticles that grow to longer nanorods [50]. The nanorods are connected by orientation attachment process, resulting in the formation of flower-shaped petals due to van der Waals driving force [51]. According to Jayanthi et al. [48] the formation of nanorods with elongated direction supports the preferential growth of ZnO structures that occurs along the direction of minimum surface free energy. However, the efficient incorporation of dopant ions into the ZnO lattice inhibited the particle growth and flower-like morphology formation. The change in morphology would then be affected by the nucleation and growth processes, which can depend on the synthesis parameters as well as on the charge of the surface states [48]. Additionally, Zamiri et al. [52] attributed the decrease in the growth rate of ZnO nanoparticles along the c-axis direction in the presence of trivalent rare earth dopant to an enhanced adsorption of OH^- ligands, which ended up preventing the deposition of Zn species onto (0001) basal surfaces. In this way, the morphological changes observed in the $Zn_{1-x}Ni_xO$ and $Zn_{1-x}Fe_xO$ samples can be related to the incorporation of these ions into the ZnO lattice.

TEM and high-resolution TEM (HRTEM) images of undoped ZnO, $Zn_{0.96}Ni_{0.04}O$ and $Zn_{0.99}Fe_{0.01}O$ powders are shown in Fig. 3. All samples exhibit particles with well-defined planes and high crystallinity as observed by selected area electron diffraction (SAED). The analysis of the interplanar distances in the selected areas of the samples shows the (103), (110), (102), (002), (100) and (004) planes corresponding to the interplanar distances of 0.159, 0.169, 0.193, 0.258, 0.282 and 0.521 nm, respectively. These planes characterize the ZnO hexagonal structure of the samples, corroborating the XRD and Raman analyzes. For the doped samples, $Zn_{0.96}Ni_{0.04}O$ and $Zn_{0.99}Fe_{0.01}O$, a preferential orientation of the rods in the (001) plane is observed when compared to the undoped ZnO sample.

3.3. Optical properties

Fig. 4 depicts the UV-visible absorption spectra of the ZnO, $Zn_{1-x}Ni_xO$ and $Zn_{1-x}Fe_xO$ samples. A weak absorption band in the visible region of 600–700 nm can be observed for the $Zn_{1-x}Ni_xO$ samples (inset of Fig. 4a). These absorption bands can be assigned to the spin–orbit split $^3T_{1(F)} \rightarrow {}^3T_{1(P)}$ ligand field transitions of the Ni^{2+} ions in the tetrahedral coordination [53]. Fig. 4b shows the absorption spectra of the $Zn_{1-x}Fe_xO$ samples. The broad absorption band around 400–600 nm can be attributed to the d–d crystal-field transitions between multiplets of $3d^5$ configuration of the high spin Fe^{3+} in the ZnO matrix, indicating that the Fe^{3+} ions were substitutionally incorporated into the tetrahedral sites [54]. These transitions are assigned from the $^6A_{1g}$ ground state to $^4T_1$, $^4T_2$, ^4E, and $^4A_1$ excited states [54]. The ZnO, $Zn_{1-x}Ni_xO$ and $Zn_{1-x}Fe_xO$ samples presented similar band gap values of E_{gap}= 3.4 eV, as observed by the optical band gap energies determined using the Kubelka–Munk formula, as shown in supporting information, Fig. S2.

All samples showed photoluminescent broad emission bands in the orange-red visible region as shown in Fig. 5. The visible emission in ZnO is sensitive to the different types of defects generated. For instance, the

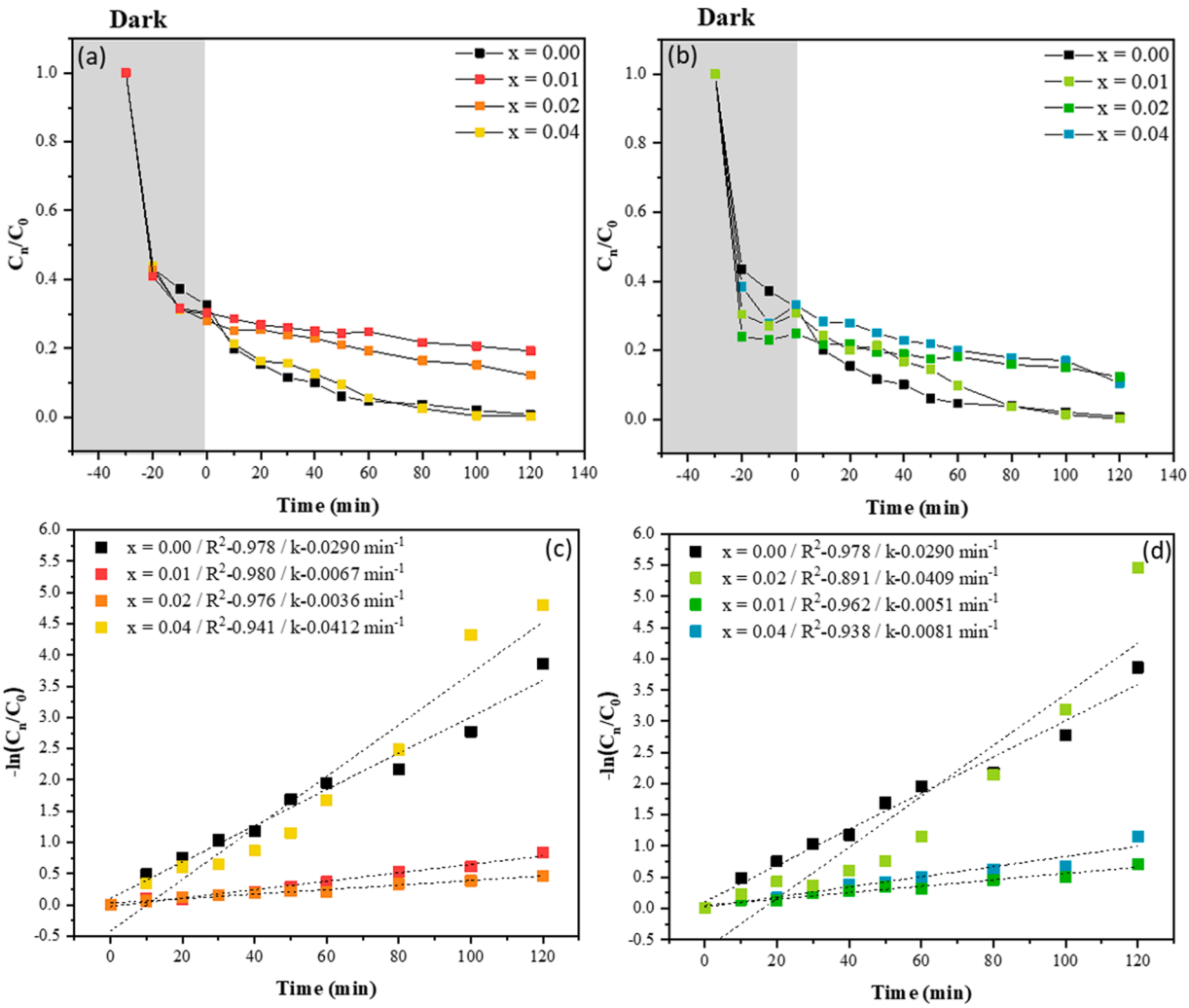

Fig. 7. Curves of photodegradation of 4-NP using (a) $Zn_{1-x}Ni_xO$ (b) $Zn_{1-x}Fe_xO$ (x=0.01; 0.02 and 0.04 mol) photocatalysts under UV-vis irradiation. Rate constant, k, (-ln C/C_0) as a function of irradiation time using (c) $Zn_{1-x}Ni_xO$ (d) $Zn_{1-x}Fe_xO$ photocatalysts; x= mol of Ni^{2+} or Fe^{3+}.

green luminescence in ZnO is commonly attributed to singly V_o, while the orange-red emissions are assigned to oxygen interstitials (O_i) [27, 55]. In this work, the broad emission band intensity in the orange-red visible region decreases with the insertion of Ni^{2+} ions and increases with the incorporation of higher concentrations of this ion into the oxide lattice, suggesting an ordering of the crystalline lattice of ZnO with the substitution of [ZnO_6] for [NiO_6] clusters, followed by a disorder effect due to the interference caused by the excess of [NiO_6] clusters (Fig. 5a). For Fe^{3+}-doped samples, the opposite effect is observed, with a decrease in the photoluminescent emission intensity, caused by the local order induced by [FeO_6] clusters (Fig. 5b). Similar results were reported in the literature [56–59]. According to these studies, the incorporation of metallic ions into the host matrix increases the density of structural defects and favors the formation of lower energy levels in the conduction band of the semiconductor. For instance, the presence of Fe^{3+} ions decreases the number of V_o and O_i ions compared to undoped ZnO due to the formation of local defects represented by one cation vacancy (V''_{Zn}) every two Fe^{3+} dopant ions in order to charge balance [56]. Upon Ni^{2+} incorporation, the intensity of PL emission also increases because of distortion centers in the ZnO lattice resulting from the presence of [NiO_6] clusters [60]. The interaction between the dopant ions and the host semiconductor contributes to the separation of electron–hole pairs, which can be subsequently related to their photocatalytic activity [61]. The deconvolution of PL spectra was carried out from two components, at 578 and at 680 nm, referring to shallow and deep defects in the samples, respectively (Table S3). As dopants provide adverse effects in terms of intensity, this is also reflected in the deconvolution of characteristic emissions. The insertion of a higher concentration of dopant causes an increase in the density of deep defects (V_o) in $Zn_{1-x}Ni_xO$ samples and a decrease in the $Zn_{1-x}Fe_xO$ samples. Such control of defects in a semiconductor becomes essential when exploring its potential for photodegradation since the photocatalytic activity is intrinsically linked to the defects in the sample [62].

3.4. Photocatalytic degradation of rhodamine-B and 4-nitrophenol

Undoped ZnO, $Zn_{1-x}Ni_xO$ and $Zn_{1-x}Fe_xO$ samples were used as photocatalysts for the degradation of model RhB molecules with initial concentration of $C_0 = 1\times10^{-5}$ mol L^{-1}. The photocatalysts were irradiated under ultraviolet light, followed by UV-vis analysis to estimate the concentration of remaining RhB. It could be observed that the characteristic absorption band of RhB (at 554 nm) decreases as a result of the gradual de-ethylation of the functional groups N,N'-diethylammonium, causing the color to change from pink to transparent [63].

The photodegradation results show the concentration of RhB (C_n/C_0) as a function of irradiation time, where C_n is the concentration over time and C_0 the initial concentration, respectively (Fig. 6a,b). For all samples, a stabilization of surface adsorptive processes is observed after 30 min in the dark. The undoped ZnO presents adsorption of approximately 14%, while the $Zn_{1-x}Ni_xO$ and $Zn_{1-x}Fe_xO$ samples present higher adsorption

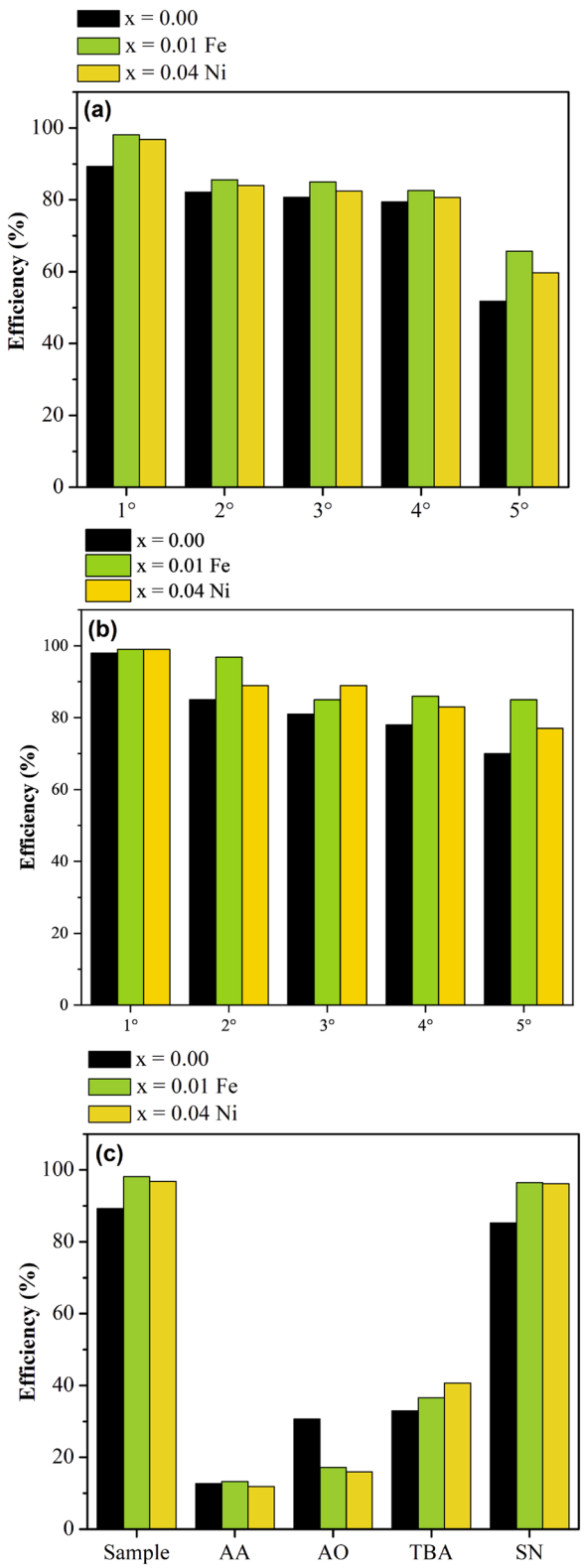

Fig. 8. (a) Recycles of RhB and (b) recycles of 4-NP photodegradation. **(c) S**cavenger tests using L-ascorbic acid (AA), ammonium oxalate (AO), tert-butyl alcohol (TBA) and silver nitrate (SN) for undoped ZnO, $Zn_{0.96}Ni_{0.04}O$ and $Zn_{0.99}Fe_{0.01}O$ samples.

values (between 16 and 23%). During the photocatalytic process of $Zn_{1-x}Ni_xO$ samples doped with higher concentrations of Ni^{2+}, there is a favoring photodegradation process for RhB. The opposite effect is observed for the $Zn_{1-x}Fe_xO$ samples, that is, their photocatalytic efficiency is improved with the decrease of the Fe^{3+} concentration. For the degradation of 4-NP solutions (10 ppm), tests similar to those of RhB were performed. A reduction in the absorption band characteristic of 4-NP was observed at 317 nm. After stabilization of the adsorption (30 min in the dark), high adsorption values of 4-NP (~70%) are observed for all samples (Fig. 7a,b). This is due to the interaction of the surface charges of the ZnO samples with the 4-NP [64,65]. In line with the results obtained for RhB, for the photodegradation of 4-NP, the sample with the highest concentration of Ni^{2+} favors the photocatalytic process, as well as the one with the lowest concentration of Fe^{3+}. According to the PL results, the V_o have a fundamental role in the generation of e^-/h^+ pairs, not only because they act as electron trapping centers, but also because they create intermediate levels in the forbidden region of the band gap, consequently making electronic excitation easier through ultraviolet light irradiation [62,66–68]. Thus, the photocatalytic efficiency is mostly related to local order/disorder effects caused by the concentration of dopants in the ZnO lattice [69,70].

Most heterogeneous photocatalytic mechanisms for semiconductors are considered pseudo-first order reactions, as a result of the low initial dye concentration and constant catalyst concentration [71]. Herein, we used the Langmuir−Hinshelwood (L−H) kinetic model to obtain the kinetic constants of the photodegradation reaction (Fig. 6c,d) [72,73]. For all samples, a R^2 greater than 0.89 was obtained, indicating that the kinetic model used was suitable for the photodegradation of RhB [74]. For RhB (Fig. 6c,d) the photodegradation rate of the $Zn_{0.96}Ni_{0.04}O$ (k=0.0551 min^{-1}) and $Zn_{0.99}Fe_{0.01}O$ (k = 0.0642 min^{-1}) samples were higher, the k values obtained for these samples are higher when compared to the undoped ZnO sample (k = 0.0340 min^{-1}). The same occurs for the photodegradation of 4-NP (Fig. 7c,d), obtaining higher k values for $Zn_{0.96}Ni_{0.04}O$ (k = 0.0412 min^{-1}) and $Zn_{0.99}Fe_{0.01}O$ (k = 0.0409 min^{-1}), than for pure ZnO (k = 0.0290 min^{-1}).

The stability of the catalysts was tested by successive recycles of RhB and 4-NP photodegradation and compared to the ZnO sample (Fig. 8a, b). A gradual reduction in efficiency was observed for all samples. In the 5th cycle, the RhB photodegradation activity of ZnO was found to be 52%, while for the $Zn_{0.99}Fe_{0.01}O$ and $Zn_{0.96}Ni_{0.04}O$ for samples this value was 66% and 60%, respectively. In the case of 4-NP, in the 5th cycle the photodegradation/adsorption efficiency for ZnO was 70%, while for the $Zn_{0.99}Fe_{0.01}O$ and $Zn_{0.96}Ni_{0.04}O$ samples this value was 85% and 77%, respectively. The DRX and FE-SEM analyses after RhB photodegradation (supporting information, Fig. S3 and S4) did not show significant differences in the samples before and after the photodegradation recycles. The efficiency loss between 40 and 15% is related to mass loss and photocorrosion processes to which the ZnO was submitted during the cycles [75,76].

The photocatalysis process is intrinsically linked to the formation of photogenerated e^-/h^+ pairs and their interaction with molecules available in the surrounding chemical environment, as well to their interaction with the water molecules of the solvent and molecular oxygen, giving rise to $^{\bullet}OH$ and $^{\bullet}O_2^-$ radicals, respectively. Therefore, to elucidate the role of such species in the degradation mechanisms, scavengers were used to eliminate the effect of the respective species on the RhB degradation process. Tert-butyl alcohol (TBA), L-ascorbic acid (AA), silver nitrate (SN) and ammonium oxalate (AO) were used as scavengers for $^{\bullet}OH$, $^{\bullet}O_2^-$, e^- and h^+, respectively (Fig. 8c) [77,78]. An abrupt reduction in the photocatalytic efficiency using AA, AO and TBA indicates that the photocatalysis process occur via $^{\bullet}O_2^-$, h^+ and $^{\bullet}OH$. These species end up interacting with RhB, causing colorless and lower molecular weight organic compounds to be created, or even mineralized. The intermediate states created in the band gap region by doping with Ni^{2+} and Fe^{3+} facilitate electronic promotion, besides acting as e^- traps [79–82].

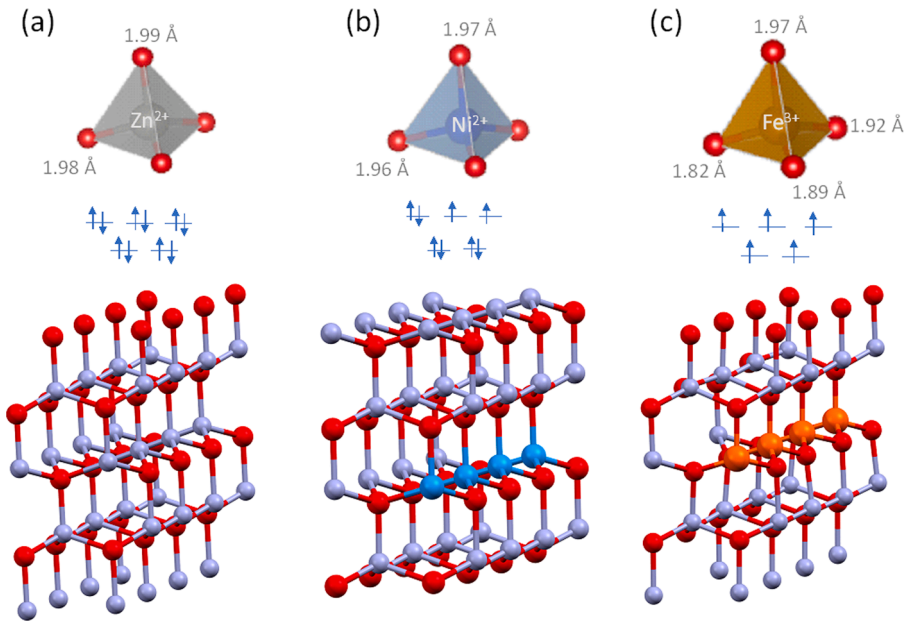

Fig. 9. Schematic representation of the [ZnO_4] cluster in the (a) undoped ZnO wurtzite structure and (b) the [NiO_4] and (c) [FeO_4] clusters in the doped ZnO, with indication of the metal-oxygen bonding lengths and the respective metal electronic configuration. The gray, blue and orange spheres represent Zn^{2+}, Ni^{2+}, and Fe^{3+} cations, respectively while the red spheres correspond to oxygen anions.

3.5. Theoretical study of $Zn_{1-x}Ni_xO$ and $Zn_{1-x}Fe_xO$ structures

To elucidate the different photocatalytic performances achieved by the Ni^{2+} and Fe^{3+} doping process on the electronic structure of ZnO, studies based on the density functional theory were carried out. Fig. 9a–c present the local organization of the [ZnO_4] cluster in the undoped ZnO wurtzite structure, as well of the [NiO_4] and [FeO_4] clusters formed in each doped sample. The Ni^{2+}, which has ionic radius of 0.55 Å, substitutes the Zn^{2+} (0.60 Å) in the structure, maintaining similar bond lengths, whereas the substitution of Zn^{2+} by Fe^{3+} (0.49 Å) provokes a greater structural distortion. For the $Zn_{1-x}Fe_xO$ system, the resulting compressed cluster can be attributed to the smaller ionic radius of Fe^{3+} with respect to Zn^{2+} and to the higher charge, which is capable of generating additional attractive forces with the oxygen anions.

The presence of transition metals such as Ni^{2+} and Fe^{3+}, in the ZnO matrix show potential to generate magnetic susceptibility due to the existence of unpaired electrons [83–85]. Under the influence of tetrahedral crystal field of wurtzite ZnO, as depicted in Fig. 9, the splitting of 3d states results in lower e_g states and higher t_{2g} [86–88]. To consider these effects in the electronic properties, ferromagnetic (FM) and antiferromagnetic (AFM) $Zn_{1-x}Ni_xO$ and $Zn_{1-x}Fe_xO$ structures were calculated. From the band structure (BS) of the wurtzite ZnO, exhibited in supporting information Fig. S5, it is seen that the system shows a direct band gap of 3.67 eV, being 0.23 eV higher than the experimental value of 3.4 eV. For each dopant, different aspects can be observed. For instance, the BS of the doped systems (supporting information, Fig. S5) indicates a decreased band gap for Ni^{2+} doping. On the other hand, for the Fe^{3+}-doped ZnO system the VB band moves to higher energies and the CB band moves to higher energy direction, resulting in an increased band gap.

In Fig. 10a, the density of states (DOS) indicates that for the ZnO system, the top of the VB is derived mainly from O 2sp orbitals and Zn 3d orbitals, while the bottom of the CB arises from Zn 4sp orbitals. Furthermore, the completely symmetrical spin DOS of ZnO demonstrates the non-magnetism of the undoped oxide. In Fig. 10b,e, the asymmetry observed in the spin polarized DOS reveals the ferromagnetism by virtue of the insertion of dopant 3d electrons. Due to the action of the tetrahedral crystalline field, the 3d orbitals of the dopant splits, and the band structure is modified. The resulting t_{2g} states hybridize with O 2p orbitals and further split into lower t-bonding states and higher t-antibonding states [86,89].

The addition of Ni^{2+} and Fe^{3+} cations as dopant elements in the ZnO lattice generates significant impurity states within the band gap of the ZnO system. For each dopant different aspects can be observed in the DOS diagrams (Fig. 10b–e). The Ni^{2+} insertion renders additional levels, mainly in the top of the VB in both FM and AFM ordering, showing contributions in the CB, which is major in the AFM system (Fig. 10b,c). In the >Fig. 10d,e, the DOS indicates expressive contribution of Fe 3d orbitals in the bottom of the CB for spin down electrons and a strong hybridization between Fe-3d and O-2sp orbitals in the VB, resulting in shallow traps and improved carrier separation. For the AFM structure (Fig. 10d) an intermediary level located 3 eV above VB is formed for the spin down electrons.

The calculated electronic structure for the $Zn_{1-x}Ni_xO$ and $Zn_{1-x}Fe_xO$ systems demonstrates that the impurity energy level comprises new paths, which certainly affects the e^-/h^+ pair formation. These impurities facilitate transitions from VB to CB levels, influencing charge separation and recombination mechanisms. With the insertion of Ni^{2+} and Fe^{3+} dopant cations, localized new energy levels emerge within the ZnO band gap. The 3d orbital splitting occurs in different magnitudes due to the different electronic configuration of each dopant, influencing the transition energies in the tetrahedral ZnO environment. For Fe^{3+}, the half-filled 3d orbital generates levels below the CB, whereas for Ni^{2+}, owning $3d^8$ configuration, the levels spread in a broad energy range above the VB.

During the photoexcitation process, electrons are easily transferred from the VB of ZnO to the localized energy levels of Ni^{2+} or Fe^{3+}, leaving h^+ in the VB. The excited e^-, which are trapped in the dopant energy levels and the h^+, may migrate to the photocatalyst surface for the generation of reactive species responsible for the pollutant decomposition. As verified by the experimental results, the doping percentages affected the efficiency of the photocatalyst performance in an intricate form. When the Ni^{2+} doping concentration was increased, an improved photocatalytic activity was achieved, while the opposite was true for Fe^{3+} doping, that is, lower Fe^{3+} doping concentration showed best results. Dhiman et al. prepared ZnO:Ni:Fe nanocomposites containing 1%, 3% and 5% of Fe^{3+} and observed an increase in the photocatalytic response from 1% to 3% Fe^{3+}; however, at 5% of Fe^{3+} the sample

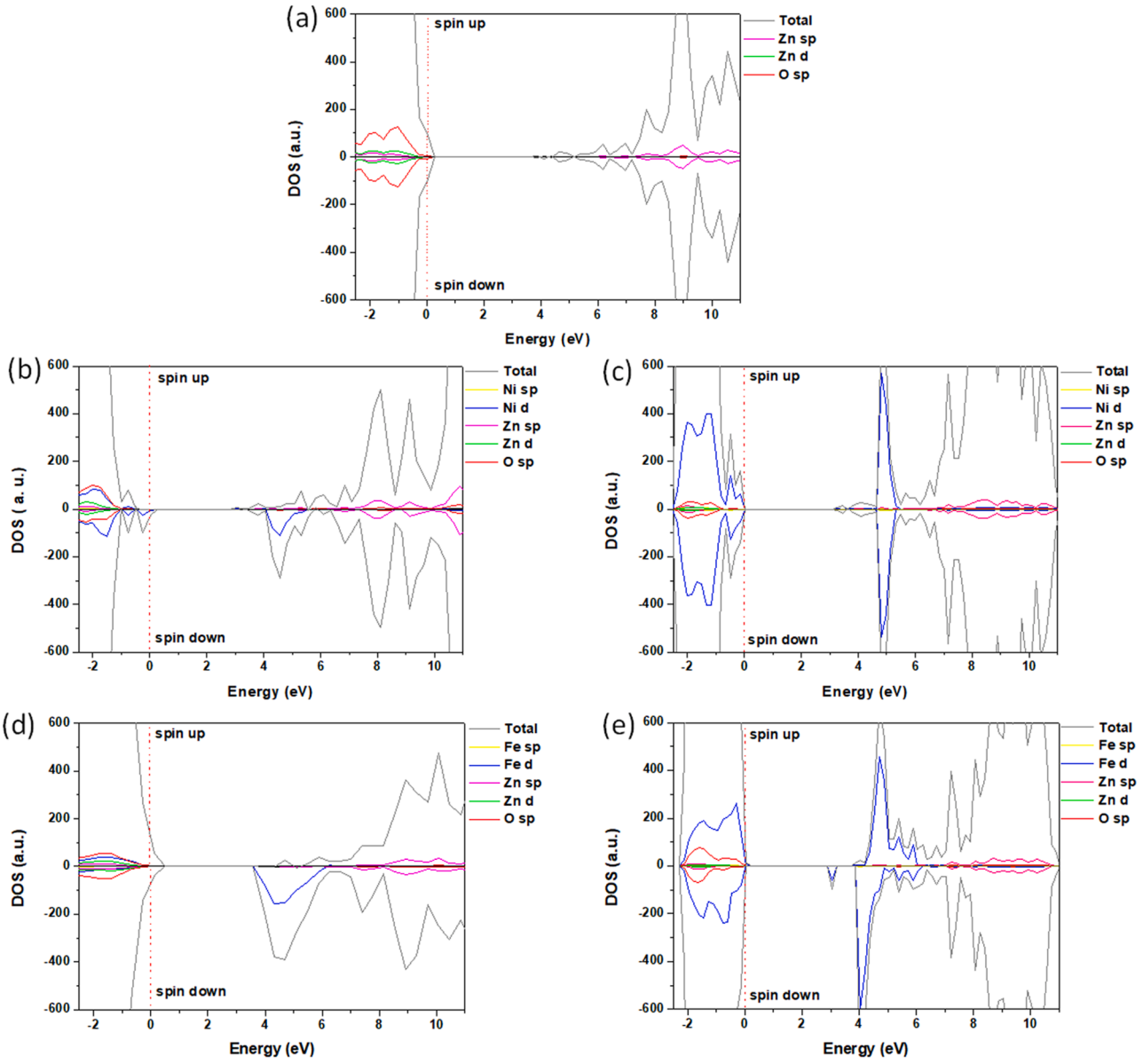

Fig. 10. Spin-polarized DOS diagram of (a) ZnO (b) ferromagnetic and (c) antiferromagnetic $Zn_{1-x}Ni_xO$ (d) ferromagnetic and (e) antiferromagnetic $Zn_{1-x}Fe_xO$.

showed lower efficiency. These authors attributed this behavior to the presence of more cation vacancies generated by the higher content of Fe^{3+} in the structure [90]. Recently, Liu et al. [91] discussed that the excess of Fe^{3+} with Zn vacancies can decrease the photocatalyst efficiency due to the formation of impurity levels, which act as recombination centers.

Moreover, the magnetic ordering (AFM or FM) is another factor affected by the concentration of the dopant ions. In other words, as the dopant concentration increases there may be a change in the preferential magnetic coupling, thus altering the electronic properties of the system [92]. The material design goal is to reach a higher charge separation and transport along with a lower recombination rate. The best photocatalytic degradation was achieved by $Zn_{0.99}Fe_{0.01}O$ sample. The theoretical results, performed considering both FM and AFM ordering, indicates the expressive contribution of Ni 3d intra-band levels in the top of the VB, which may facilitate the photocatalytic mechanism involving the presence of h^+, as indicated by the slightly higher suppression of the degradation mechanism when the scavenger for h^+ was applied, even though the extended energy range of these levels may also favor competitive recombination paths. For the Fe^{3+} doping, greater band separation and denser levels in the CB may provide a better charge separation, reducing recombination rate and paths that efficiently boost the inter-band electron transport.

4. Conclusions

High performance $Zn_{1-x}Ni_xO$ and $Zn_{1-x}Fe_xO$ photocatalysts were successfully synthesized by the microwave-assisted hydrothermal method. The incorporation of Ni^{2+} and Fe^{3+} cations into the tetragonal coordination generated local defects within the ZnO lattice, influencing their optical and photocatalytic properties. The morphology was also affected by the decrease of the ZnO crystal growth along the c-axis direction in the presence of the dopants. The $Zn_{0.96}Ni_{0.04}O$ and $Zn_{0.99}Fe_{0.01}O$ materials exhibited high photocatalytic efficiency of 96.9 and 98.2% for the degradation of RhB, and of 99.8 and 99.1% for 4-NP, respectively, furthermore good recyclability was achieved. These enhanced performances can be related to a band structure that allows higher separation of e^-/h^+ pairs, lowering the recombination rate and to the formation of levels that efficiently boost the photocarrier transport. The theoretical calculations indicated the formation of new energy

levels due to the introduction of Ni^{2+} and Fe^{3+} ions into the ZnO lattice, which caused an impact on the e^-/h^+ pair formation, elucidating the specific electronic aspects promoted by each dopant. The remarkable degradation performance of the Ni^{2+} and Fe^{3+} doped ZnO samples provide a promising strategy to obtain catalysts for the removal of pollutants.

CRediT authorship contribution statement

Samantha Custódio Silva Lemos: Investigation, Methodology, Formal analysis, Conceptualization, Data curation, Writing – original draft, Writing – review & editing. **Thaís Karine de Lima Rezende:** Investigation, Methodology, Formal analysis, Investigation, Writing – original draft. **Marcelo Assis:** Investigation, Methodology, Formal analysis, Conceptualization, Data curation, Writing – original draft. **Fernanda da Costa Romeiro:** Methodology, Formal analysis, Data curation, Writing – original draft, Writing – review & editing. **Diego Alves Peixoto:** Investigation, Formal analysis. **Eduardo de Oliveira Gomes:** Investigation, Methodology, Formal analysis, Writing – review & editing. **Gabriel Marques Jacobsen:** Investigation, Formal analysis. **Marcio Daldin Teodoro:** Investigation, Formal analysis, Resources. **Lourdes Gracia:** Methodology, Formal analysis, Conceptualization, Data curation, Writing – original draft, Writing – review & editing. **Jefferson Luis Ferrari:** Writing – review & editing. **Elson Longo:** Conceptualization, Resources. **Juan Andrés:** Conceptualization, Resources, Visualization, Writing – review & editing. **Renata Cristina de Lima:** Supervision, Conceptualization, Funding acquisition, Project administration, Resources, Visualization, Writing – review & editing.

Declaration of Competing Interest

The authors declare that they have no known competing financial interests or personal relationships that could have appeared to influence the work reported in this paper.

Acknowledgements

This work was funded in part by Fundação de Amparo à Pesquisa do Estado de São Paulo - FAPESP (2013/07296-2), Fundação de Amparo à Pesquisa do Estado de Minas Gerais – FAPEMIG (APQ-00988-13), Rede Mineira de Química (RQ-MG), Financiadora de Estudos e Projetos - FINEP, Conselho Nacional de Desenvolvimento Cientifico e Tecnológico - CNPq (166281/2017-4 and 164227/2020-2), CAPES (finance code 001) and Grupo de Materiais Inorgânicos do Triângulo (GMIT) (Research Group supported by FAPEMIG (APQ-00330-14)) for the financial support. Marcelo Assis was supported by the Margarita Salas postdoctoral contract MGS/2021/21(UP2021-021) financed by the European Union-NextGenerationEU. J.A. acknowledges Universitat Jaume I (project UJI-B2019-30), and the Ministerio de Ciencia, Innovación y Universidades (Spain) (project PGC2018094417-B-I00) for financially supporting this research.

Supplementary materials

Supplementary material associated with this article can be found, in the online version, at doi:10.1016/j.materresbull.2022.111849.

References

[1] C.C. Wang, J.R. Li, X.L. Lv, Y.Q. Zhang, G. Guo, Photocatalytic organic pollutants degradation in metal–organic frameworks, Energy Environ. Sci. 7 (2014) 2831–2867, https://doi.org/10.1039/C4EE01299B.
[2] R. Beura, P. Thangadurai, Effect of Sn doping in ZnO on the photocatalytic activity of ZnO-Graphene nanocomposite with improved activity, J. Environ. Chem. Eng. 6 (2018) 5087–5100, https://doi.org/10.1016/j.jece.2018.07.049.
[3] D. N, K.K. Kondamareddy, H. Bin, D. Lu, P. Kumar, R.K. Dwivedi, V.O. Pelenovich, X.-Z. Zhao, W. Gao, D. Fu, Enhanced visible light photodegradation activity of RhB/MB from aqueous solution using nanosized novel Fe-Cd co-modified ZnO, Sci. Rep. 8 (2018) 10691, https://doi.org/10.1038/s41598-018-29025-1.
[4] M.R. Hoffmann, S.T. Martin, W. Choi, D.W. Bahnemann, Environmental applications of semiconductor photocatalysis, Chem. Rev. 95 (1995) 69–96, https://doi.org/10.1021/cr00033a004.
[5] M. Cheng, G. Zeng, D. Huang, C. Lai, P. Xu, C. Zhang, Y. Liu, Hydroxyl radicals based advanced oxidation processes (AOPs) for remediation of soils contaminated with organic compounds: a review, Chem. Eng. J. 284 (2016) 582–598, https://doi.org/10.1016/j.cej.2015.09.001.
[6] A. Fujishima, K. Honda, Electrochemical photolysis of water at a semiconductor electrode, Nature 238 (1972) 37–38, https://doi.org/10.1038/238037a0.
[7] M.A. Henderson, I. Lyubinetsky, Molecular-level insights into photocatalysis from scanning probe microscopy studies on TiO_2(110), Chem. Rev. 113 (2013) 4428–4455, https://doi.org/10.1021/cr300315m.
[8] A. Sadeghzadeh-Attar, Efficient photocatalytic degradation of methylene blue dye by SnO_2 nanotubes synthesized at different calcination temperatures, Sol. Energy Mater. Sol. Cells 183 (2018) 16–24, https://doi.org/10.1016/j.solmat.2018.03.046.
[9] P. Jantawasu, T. Sreethawong, S. Chavadej, Photocatalytic activity of nanocrystalline mesoporous-assembled TiO_2 photocatalyst for degradation of methyl orange monoazo dye in aqueous wastewater, Chem. Eng. J. 155 (2009) 223–233, https://doi.org/10.1016/j.cej.2009.07.036.
[10] H. Liang, Z. Jia, H. Zhang, X. Wang, J. Wang, Photocatalysis oxidation activity regulation of Ag/TiO_2 composites evaluated by the selective oxidation of Rhodamine B, Appl. Surf. Sci. 422 (2017) 1–10, https://doi.org/10.1016/j.apsusc.2017.05.211.
[11] X. Chen, Z. Wu, D. Liu, Z. Gao, Preparation of ZnO photocatalyst for the efficient and rapid photocatalytic degradation of Azo Dyes, Nanoscale Res. Lett. 12 (2017) 143, https://doi.org/10.1186/s11671-017-1904-4.
[12] S.C.S. Lemos, F.C. Romeiro, L.F. de Paula, R.F. Goncalves, A.P. de Moura, M. M. Ferrer, E. Longo, A.O.T. Patrocinio, R.C. Lima, Effect of Er^{3+} ions on the phase formation and properties of In_2O_3 nanostructures crystallized upon microwave heating, J. Solid State Chem. 249 (2017) 58, https://doi.org/10.1016/j.jssc.2017.02.011.
[13] S. Baruah, J. Dutta, Hydrothermal growth of ZnO nanostructures, Sci. Technol. Adv. Mater. 10 (2009), 013001, https://doi.org/10.1088/1468-6996/10/1/013001.
[14] J.Z. Marinho, F.C. Romeiro, S.C.S. Lemos, F.V. Motta, C.S. Riccardi, M.S. Li, E. Longo, R.C. Lima, Urea-based synthesis of zinc oxide nanostructures at low temperature, J. Nanomater. (2012) 1–7, https://doi.org/10.1155/2012/427172, 2012.
[15] K. Ravichandran, R. Mohan, B. Sakthivel, S. Varadharajaperumal, P. Devendran, T. Alagesan, K. Pandian, Enhancing the photocatalytic efficiency of sprayed ZnO thin films through double doping (Sn+F) and annealing under different ambiences, Appl. Surf. Sci. 321 (2014) 310–317, https://doi.org/10.1016/j.apsusc.2014.10.023.
[16] E. Vasilaki, I. Georgaki, D. Vernardou, M. Vamvakaki, N. Katsarakis, Ag-loaded TiO_2/reduced graphene oxide nanocomposites for enhanced visible-light photocatalytic activity, Appl. Surf. Sci. 353 (2015) 865–872, https://doi.org/10.1016/j.apsusc.2015.07.056.
[17] A. Khlyustova, N. Sirotkin, T. Kusova, A. Kraev, V. Titov, A. Agafonov, Doped TiO_2: the effect of doping elements on photocatalytic activity, Mater. Adv. 1 (2020) 1193–1201, https://doi.org/10.1039/D0MA00171F.
[18] F.C. Romeiro, J.Z. Marinho, A.C.A. Silva, N.F. Cano, N.O. Dantas, R.C. Lima, Photoluminescence and magnetism in Mn^{2+}-doped ZnO nanostructures grown rapidly by the microwave hydrothermal method, J. Phys. Chem. C 117 (2013) 26222–26227, https://doi.org/10.1021/jp408993y.
[19] N.R. Khalid, A. Hammad, M.B. Tahir, M. Rafique, T. Iqbal, G. Nabi, M.K. Hussain, Enhanced photocatalytic activity of Al and Fe co-doped ZnO nanorods for methylene blue degradation, Ceram. Int. 45 (2019) 21430–21435, https://doi.org/10.1016/j.ceramint.2019.07.132.
[20] Z. Ji, Z. Luo, J. Li, P. Li, Enhanced photocatalytic activity of ZnO toward the degradation of methylene blue dye: effects of Fe^{3+} and Sn^{4+} doping, Phys. Status Solidi 216 (2019), 1800947, https://doi.org/10.1002/pssa.201800947.
[21] S.C.S. Lemos, E. Nossol, J.L. Ferrari, E.O. Gomes, J. Andres, L. Gracia, I. Sorribes, R. C. Lima, Joint theoretical and experimental study on the la doping process in In_2O_3: phase transition and electrocatalytic activity, Inorg. Chem. 58 (2019) 11738–11750, https://doi.org/10.1021/acs.inorgchem.9b01728.
[22] L.A. Gusmão, D.A. Peixoto, J.Z. Marinho, F.C. Romeiro, R.F. Gonçalves, E. Longo, C.A. de Oliveira, R.C. Lima, Alkali influence on ZnO and Ag-doped ZnO nanostructures formation using the microwave-assisted hydrothermal method for fungicidal inhibition, J. Phys. Chem. Solids 158 (2021), 110234, https://doi.org/10.1016/j.jpcs.2021.110234.
[23] L. Qiaoping, L. Xin, Y. Yanning, Z. Fuchun, Z. Qi, Hydrothermal synthesis and optical properties of Fe doped ZnO nanorods, Ferroelectrics 564 (2020) 59–69, https://doi.org/10.1080/00150193.2020.1761702.
[24] T.C. Bharat, S. Shubham, H.S. Mondal, P.K. Gupta, A.K. Singh, Das, Synthesis of doped zinc oxide nanoparticles: a review, Mater. Today Proc. 11 (2019) 767–775, https://doi.org/10.1016/j.matpr.2019.03.041.
[25] P. Singh, R. Kumar, R.K. Singh, Progress on transition metal-doped ZnO nanoparticles and its application, Ind. Eng. Chem. Res. 58 (2019) 17130–17163, https://doi.org/10.1021/acs.iecr.9b01561.
[26] V. Vinitha, M. Preeyanghaa, V. Vinesh, R. Dhanalakshmi, B. Neppolian, V. Sivamurugan, Two is better than one: catalytic, sensing and optical applications of doped zinc oxide nanostructures, Emerg. Mater. (2021), https://doi.org/10.1007/s42247-021-00262-x.

[27] F.C. Romeiro, J.Z. Marinho, S.C.S. Lemos, A.P. de Moura, P.G. Freire, L.F. da Silva, E. Longo, R.A.A. Munoz, R.C. Lima, Rapid synthesis of Co, Ni co-doped ZnO nanoparticles: optical and electrochemical properties, J. Solid State Chem. 230 (2015) 343–349, https://doi.org/10.1016/j.jssc.2015.07.026.

[28] P. Pascariu, I.V. Tudose, M. Suchea, E. Koudoumas, N. Fifere, A. Airinei, Preparation and characterization of Ni, Co doped ZnO nanoparticles for photocatalytic applications, Appl. Surf. Sci. 448 (2018) 481–488, https://doi.org/10.1016/j.apsusc.2018.04.124.

[29] M. Ben Ali, F. Barka-Bouaifel, B. Sieber, H. Elhouichet, A. Addad, L. Boussekey, M. Férid, R. Boukherroub, Preparation and characterization of Ni-doped ZnO–SnO_2 nanocomposites: application in photocatalysis, Superlattices Microstruct. 91 (2016) 225–237, https://doi.org/10.1016/j.spmi.2016.01.014.

[30] A. Mondal, N. Giri, S. Sarkar, S. Majumdar, R. Ray, Tuning the photocatalytic activity of ZnO by TM (TM = Fe, Co, Ni) doping, Mater. Sci. Semicond. Process. 91 (2019) 333–340, https://doi.org/10.1016/j.mssp.2018.12.003.

[31] D. Neena, M. Humayun, W. Zuo, C.S. Liu, W. Gao, D.J. Fu, Hierarchical hetero-architectures of *in-situ* g-C_3N_4-coupled Fe-doped ZnO micro-flowers with enhanced visible-light photocatalytic activities, Appl. Surf. Sci. 506 (2020), 145017, https://doi.org/10.1016/j.apsusc.2019.145017.

[32] J. Theerthagiri, S. Salla, R.A. Senthil, P. Nithyadharseni, A. Madankumar, P. Arunachalam, T. Maiyalagan, H.S. Kim, A review on ZnO nanostructured materials: energy, environmental and biological applications, Nanotechnology 30 (2019), 392001, https://doi.org/10.1088/1361-6528/ab268a.

[33] T. Malevu, R. Ocaya, An investigation of nanostructure morphology in the zinc-air cell method as a function of electrolyte concentration, Int. J. Electrochem. Sci. 10 (2015) 4097–4104.

[34] S. Shahzad, S. Javed, M. Usman, A review on synthesis and optoelectronic applications of nanostructured ZnO, Front. Mater. 8 (2021), https://doi.org/10.3389/fmats.2021.613825.

[35] J. Wojnarowicz, T. Chudoba, W. Lojkowski, A review of microwave synthesis of zinc oxide nanomaterials: reactants, process parameters and morphologies, Nanomaterials 10 (2020) 1086, https://doi.org/10.3390/nano10061086.

[36] A. Hui, J. Ma, J. Liu, Y. Bao, J. Zhang, Morphological evolution of Fe doped sea urchin-shaped ZnO nanoparticles with enhanced photocatalytic activity, J. Alloys Compd. 696 (2017) 639–647, https://doi.org/10.1016/j.jallcom.2016.10.319.

[37] G. Byzynski, C. Melo, D.P. Volanti, M.M. Ferrer, A.F. Gouveia, C. Ribeiro, J. Andrés, E. Longo, The interplay between morphology and photocatalytic activity in ZnO and N-doped ZnO crystals, Mater. Des. 120 (2017) 363–375, https://doi.org/10.1016/j.matdes.2017.02.020.

[38] J.P. Perdew, M. Ernzerhof, K. Burke, Rationale for mixing exact exchange with density functional approximations, J. Chem. Phys. 105 (1996) 9982–9985, https://doi.org/10.1063/1.472933.

[39] S. Dovesi, R.; Saunders, V. R.; Roetti, C.; Orlando, C. M.; Zicovich- Wilson, C. M.; Pascale, F.; Civalleri, B.; Doll, K.; Harrison, N. M.; Bush, I. J.; D'Arco, P.; Llunell, M.; Causà, M., Noël, Y.; Maschio, L.; Erba, A.; Rerat, M.; Casassa, CRYSTAL17 User's Manual, (2018).

[40] T. Bredow, K. Jug, R.A. Evarestov, Electronic and magnetic structure of $ScMnO_3$, Phys. Status Solidi B 243 (2006) R10, https://doi.org/10.1002/pssb.200541403.

[41] T. Homann, U. Hotje, M. Binnewies, A. Börger, K.-D. Becker, T. Bredow, Composition-dependent band gap in $Zn_{Sx}Se_{1-x}$: a combined experimental and theoretical study, Solid State Sci. 8 (2006) 44–49, https://doi.org/10.1016/j.solidstatesciences.2005.08.015.

[42] M. Catti, G. Valerio, R. Dovesi, Theoretical study of electronic, magnetic, and structural properties of α-Fe_2O_3 (hematite), Phys. Rev. B 51 (1995) 7441–7450, https://doi.org/10.1103/PhysRevB.51.7441.

[43] M.D. Towler, N.L. Allan, N.M. Harrison, V.R. Saunders, W.C. Mackrodt, E. Aprà, Ab initio study of MnO and NiO, Phys. Rev. B 50 (1994) 5041–5054, https://doi.org/10.1103/PhysRevB.50.5041.

[44] S. Horzum, F. Iyikanat, R.T. Senger, C. Çelebi, M. Sbeta, A. Yildiz, T. Serin, Monitoring the characteristic properties of Ga-doped ZnO by Raman spectroscopy and atomic scale calculations, J. Mol. Struct. 1180 (2019) 505–511, https://doi.org/10.1016/j.molstruc.2018.11.064.

[45] V. Russo, M. Ghidelli, P. Gondoni, C.S. Casari, A.Li Bassi, Multi-wavelength Raman scattering of nanostructured Al-doped zinc oxide, J. Appl. Phys. 115 (2014) 73508, https://doi.org/10.1063/1.4866322.

[46] R. Zhang, P.G. Yin, N. Wang, L. Guo, Photoluminescence and Raman scattering of ZnO nanorods, Solid State Sci. 11 (2009) 865–869, https://doi.org/10.1016/j.solidstatesciences.2008.10.016.

[47] S. Karamat, R.S. Rawat, P. Lee, T.L. Tan, R.V Ramanujan, Structural, elemental, optical and magnetic study of Fe doped ZnO and impurity phase formation, Prog. Nat. Sci. Mater. Int. 24 (2014) 142–149, https://doi.org/10.1016/j.pnsc.2014.03.009.

[48] K. Jayanthi, S. Chawla, K.N. Sood, M. Chhibara, S. Singh, Dopant induced morphology changes in ZnO nanocrystals, Appl. Surf. Sci. 255 (2009) 5869–5875, https://doi.org/10.1016/j.apsusc.2009.01.032.

[49] R. Al-Gaashani, S. Radiman, A.R. Daud, N. Tabet, Y. Al-Douri, XPS and optical studies of different morphologies of ZnO nanostructures prepared by microwave methods, Ceram. Int. 39 (2013) 2283–2292, https://doi.org/10.1016/j.ceramint.2012.08.075.

[50] P. Hemalatha, S.N. Karthick, K.V Hemalatha, M. Yi, H.-J. Kim, M. Alagar, La-doped ZnO nanoflower as photocatalyst for methylene blue dye degradation under UV irradiation, J. Mater. Sci. Mater. Electron. 27 (2016) 2367–2378, https://doi.org/10.1007/s10854-015-4034-8.

[51] K.J.M. Bishop, C.E. Wilmer, S. Soh, B.A. Grzybowski, Nanoscale forces and their uses in self-assembly, Small. 5 (2009) 1600–1630. 10.1002/smll.200900358.

[52] R. Zamiri, A.F. Lemos, A. Reblo, H.A. Ahangar, J.M.F. Ferreira, Effects of rare-earth (Er, La and Yb) doping on morphology and structure properties of ZnO nanostructures prepared by wet chemical method, Ceram. Int. 40 (2014) 523–529, https://doi.org/10.1016/j.ceramint.2013.06.034.

[53] R. Elilarassi, G. Chandrasekaran, Structural, optical and magnetic properties of nanoparticles of ZnO:Ni—DMS prepared by sol–gel method, Mater. Chem. Phys. 123 (2010) 450–455, https://doi.org/10.1016/j.matchemphys.2010.04.039.

[54] J.J. Beltrán, C.A. Barrero, A. Punnoose, Understanding the role of iron in the magnetism of Fe doped ZnO nanoparticles, Phys. Chem. Chem. Phys. 17 (2015) 15284–15296, https://doi.org/10.1039/C5CP01408E.

[55] G. Srinet, R. Kumar, V. Sajal, Structural, optical, vibrational, and magnetic properties of sol-gel derived Ni doped ZnO nanoparticles, J. Appl. Phys. 114 (2013) 33912, https://doi.org/10.1063/1.4813868.

[56] M. Cernea, V. Mihalache, E.C. Secu, R. Trusca, V. Bercu, L. Diamandescu, Structural, morphological, ferromagnetic and photoluminescence properties of Fe-doped ZnO, prepared by hydrothermal route, Superlatt. Microstruct. 104 (2017) 362–373, https://doi.org/10.1016/j.spmi.2017.02.048.

[57] M. Ashokkumar, S. Muthukumaran, Effect of Ni doping on electrical, photoluminescence and magnetic behavior of Cu doped ZnO nanoparticles, J. Lumin. 162 (2015) 97–103, https://doi.org/10.1016/j.jlumin.2015.02.019.

[58] J.K. Salem, T.M. Hammad, R.R. Harrison, Synthesis, structural and optical properties of Ni-doped ZnO micro-spheres, J. Mater. Sci. Mater. Electron. 24 (2013) 1670–1676, https://doi.org/10.1007/s10854-012-0994-0.

[59] X. Liu, J. Zhang, L. Wang, T. Yang, X. Guo, S. Wu, S. Wang, 3D hierarchically porous ZnO structures and their functionalization by Au nanoparticles for gas sensors, J. Mater. Chem. 21 (2011) 349–356, https://doi.org/10.1039/C0JM01800G.

[60] I. Loyola Poul Raj, A. Jegatha Christy, R. David Prabu, N. Chidhambaram, M. Shkir, S. AlFaify, A. Khan, Significance of Ni doping on structure-morphology-photoluminescence, optical and photocatalytic activity of CBD grown ZnO nanowires for opto-photocatalyst applications, Inorg. Chem. Commun. 119 (2020), 108082, https://doi.org/10.1016/j.inoche.2020.108082.

[61] M. Yarahmadi, H. Maleki-Ghaleh, M.E. Mehr, Z. Dargahi, F. Rasouli, M.H. Siadati, Synthesis and characterization of Sr-doped ZnO nanoparticles for photocatalytic applications, J. Alloys Compd. 853 (2021), 157000, https://doi.org/10.1016/j.jallcom.2020.157000.

[62] F. Kayaci, S. Vempati, I. Donmez, N. Biyikli, T. Uyar, Role of zinc interstitials and oxygen vacancies of ZnO in photocatalysis: a bottom-up approach to control defect density, Nanoscale 6 (2014) 10224–10234, https://doi.org/10.1039/C4NR01887G.

[63] A.C.M. Tello, M. Assis, R. Menasce, A.F. Gouveia, V. Teodoro, N. Jacomaci, M. A. Zaghete, J. Andrés, G.E. Marques, M.D. Teodoro, A.B.F. da Silva, J. Bettini, E. Longo, Microwave-driven hexagonal-to-monoclinic transition in BiPO4: an in-depth experimental investigation and first-principles study, Inorg. Chem. 59 (2020) 7453–7468, https://doi.org/10.1021/acs.inorgchem.0c00181.

[64] P. Bhatia, M. Nath, Green synthesis of p-NiO/n-ZnO nanocomposites: Excellent adsorbent for removal of congo red and efficient catalyst for reduction of 4-nitrophenol present in wastewater, J. Water Process Eng. 33 (2020), 101017, https://doi.org/10.1016/j.jwpe.2019.101017.

[65] M. Khairy, E.M. Naguib, M.M. Mohamed, Enhancement of photocatalytic and sonophotocatalytic degradation of 4-nitrophenol by ZnO/Graphene oxide and ZnO/Carbon nanotube nanocomposites, J. Photochem. Photobiol. A Chem. 396 (2020), 112507, https://doi.org/10.1016/j.jphotochem.2020.112507.

[66] L. Jing, F. Yuan, H. Hou, B. Xin, W. Cai, H. Fu, Relationships of surface oxygen vacancies with photoluminescence and photocatalytic performance of ZnO nanoparticles, Sci. China Ser. B Chem. 48 (2005) 25–30, https://doi.org/10.1007/BF02990909.

[67] J. Wang, Z. Wang, B. Huang, Y. Ma, Y. Liu, X. Qin, X. Zhang, Y. Dai, Oxygen vacancy induced band-gap narrowing and enhanced visible light photocatalytic activity of ZnO, ACS Appl. Mater. Interfaces 4 (2012) 4024–4030, https://doi.org/10.1021/am300835p.

[68] L.G. da Trindade, G.B. Minervino, A.B. Trench, M.H. Carvalho, M. Assis, M.S. Li, A. J.A. de Oliveira, E.C. Pereira, T.M. Mazzo, E. Longo, Influence of ionic liquid on the photoelectrochemical properties of ZnO particles, Ceram. Int. 44 (2018) 10393–10401, https://doi.org/10.1016/j.ceramint.2018.03.053.

[69] H. Zeng, W. Cai, P. Liu, X. Xu, H. Zhou, C. Klingshirn, H. Kalt, ZnO-based hollow nanoparticles by selective etching: elimination and reconstruction of metal−semiconductor interface, improvement of blue emission and photocatalysis, ACS Nano 2 (2008) 1661–1670, https://doi.org/10.1021/nn800353q.

[70] P. Molaei, M. Cheraghizade, R. Yousefi, Impact of {rGO} on photocatalytic performance of Cd-doped {ZnO} nanostructures synthesized via a simple aqueous co-precipitation route, Mater. Res. Express. 6 (2018) 25051, https://doi.org/10.1088/2053-1591/aaf1d9.

[71] W. Baran, E. Adamek, A. Makowski, The influence of selected parameters on the photocatalytic degradation of azo-dyes in the presence of TiO_2 aqueous suspension, Chem. Eng. J. 145 (2008) 242–248, https://doi.org/10.1016/j.cej.2008.04.021.

[72] M. Assis, F.C. Groppo Filho, D.S. Pimentel, T. Robeldo, A.F. Gouveia, T.F.D. Castro, H.C.S. Fukushima, C.C. de Foggi, J.P.C. da Costa, R.C. Borra, J. Andrés, E. Longo, Ag nanoparticles/AgX (X=Cl, Br and I) composites with enhanced photocatalytic activity and low toxicological effects, ChemistrySelect 5 (2020) 4655–4673, https://doi.org/10.1002/slct.202000502.

[73] M. Assis, C.C. de Foggi, V. Teodoro, J.P. de Campos da Costa, C.E. Silva, T. Robeldo, P.F. Caperucci, C.E. Vergani, R.C. Borra, I. Sorribes, A.F. Gouveia, M. A. San-Miguel, J. Andrés, E. Longo, Surface-dependent photocatalytic and biological activities of Ag_2CrO_4: Integration of experiment and simulation, Appl. Surf. Sci. 545 (2021), 148964, https://doi.org/10.1016/j.apsusc.2021.148964.

[74] A.E.B. Lima, R.Y.N. Reis, L.S. Ribeiro, L.K. Ribeiro, M. Assis, R.S. Santos, C.H. M. Fernandes, L.S. Cavalcante, E. Longo, J.A.O. Osajima, G.E. Luz, Microwave-assisted hydrothermal synthesis of $CuWO_4$-palygorskite nanocomposite for enhanced visible photocatalytic response, J. Alloys Compd. 863 (2021), 158731, https://doi.org/10.1016/j.jallcom.2021.158731.

[75] H. Fu, T. Xu, S. Zhu, Y. Zhu, Photocorrosion inhibition and enhancement of photocatalytic activity for ZnO via hybridization with C60, Environ. Sci. Technol. 42 (2008) 8064–8069, https://doi.org/10.1021/es801484x.

[76] C. Han, M.Q. Yang, B. Weng, Y.J. Xu, Improving the photocatalytic activity and anti-photocorrosion of semiconductor ZnO by coupling with versatile carbon, Phys. Chem. Chem. Phys. 16 (2014) 16891–16903, https://doi.org/10.1039/C4CP02189D.

[77] L.P. Oliveira, C.C. de Foggi, B.N.A. da Silva Pimentel, M. Assis, J. Andrés, E. Longo, C.E. Vergani, Increasing the photocatalytic and fungicide activities of Ag_3PO_4 microcrystals under visible-light irradiation, Ceram. Int. (2021), https://doi.org/10.1016/j.ceramint.2021.04.272.

[78] M. Assis, T. Robeldo, C.C. Foggi, A.M. Kubo, G. Mínguez-Vega, E. Condoncillo, H. Beltran-Mir, R. Torres-Mendieta, J. Andrés, M. Oliva, C.E. Vergani, P. A. Barbugli, E.R. Camargo, R.C. Borra, E. Longo, Ag Nanoparticles/α-Ag_2WO_4 composite formed by electron beam and femtosecond irradiation as potent antifungal and antitumor agents, Sci. Rep. 9 (2019) 9927, https://doi.org/10.1038/s41598-019-46159-y.

[79] R. Saleh, N.F. Djaja, UV light photocatalytic degradation of organic dyes with Fe-doped ZnO nanoparticles, Superlatt. Microstruct. 74 (2014) 217–233, https://doi.org/10.1016/j.spmi.2014.06.013.

[80] W. Bousslama, H. Elhouichet, M. Férid, Enhanced photocatalytic activity of Fe doped ZnO nanocrystals under sunlight irradiation, Optik 134 (2017) 88–98, https://doi.org/10.1016/j.ijleo.2017.01.025 (Stuttg).

[81] J. Zhao, L. Wang, X. Yan, Y. Yang, Y. Lei, J. Zhou, Y. Huang, Y. Gu, Y. Zhang, Structure and photocatalytic activity of Ni-doped ZnO nanorods, Mater. Res. Bull. 46 (2011) 1207–1210, https://doi.org/10.1016/j.materresbull.2011.04.008.

[82] M.S. Abdel-wahab, A. Jilani, I.S. Yahia, A.A. Al-Ghamdi, Enhanced the photocatalytic activity of Ni-doped ZnO thin films: morphological, optical and XPS analysis, Superlatt. Microstruct. 94 (2016) 108–118, https://doi.org/10.1016/j.spmi.2016.03.043.

[83] Y. Hu, C. Ji, X. Wang, J. Huo, Q. Liu, Y. Song, The structural, magnetic and optical properties of $TM_n@(ZnO)_{42}$ (TM = Fe, Co and Ni) hetero-nanostructure, Sci. Rep. 7 (2017) 16485, https://doi.org/10.1038/s41598-017-16532-w.

[84] K. Yim, J. Lee, D. Lee, M. Lee, E. Cho, H.S. Lee, H.-H. Nahm, S. Han, Property database for single-element doping in ZnO obtained by automated first-principles calculations, Sci. Rep. 7 (2017) 40907, https://doi.org/10.1038/srep40907.

[85] L. Li, H. Liu, X. Luo, X. Zhang, W. Wang, Y. Cheng, Q. Song, Ferromagnetism in polycrystalline Cr-doped ZnO films: experiment and theory, Solid State Commun. 146 (2008) 420–424, https://doi.org/10.1016/j.ssc.2008.03.024.

[86] H. Katayama-Yoshida, K. Sato, Materials design for semiconductor spintronics by ab initio electronic-structure calculation, Phys. B Condens. Matter. 327 (2003) 337–343, https://doi.org/10.1016/S0921-4526(02)01782-9.

[87] H.A. Weakliem, Optical spectra of Ni^{2+}, Co^{2+}, and Cu^{2+} in tetrahedral sites in crystals, J. Chem. Phys. 36 (1962) 2117–2140, https://doi.org/10.1063/1.1732840.

[88] T.K. Vien, J.L. Dormann, H.Le gall, Crystal field splitting in octahedral and tetrahedral symmetry for Fe^{3+} Ions in $Y_3Fe_50_{12}$, Phys. Status Solidi. 71 (1975) 731–739, https://doi.org/10.1002/pssb.2220710235.

[89] B. Deng, Z. Guo, H. Sun, Theoretical study of Fe-doped p-type ZnO, Appl. Phys. Lett. 96 (2010), 172106, https://doi.org/10.1063/1.3422486.

[90] P.G.K. Dhiman, K.M. Batoo, A. Kumar, G. Sharma, M. Singh, Effective Degradation of Methylene Blue using ZnO:Fe:Ni Nanocomposites, in: Organic Pollutants in Wastewater I Methods of Analysis, Removal and Treatment, Materials Research Foundations, 2015, pp. 67–87.

[91] R. Liu, Y. Zhang, L. Duan, X. Zhao, Effect of Fe^{2+}/Fe^{3+} ratio on photocatalytic activities of $Zn_{1-x}Fe_xO$ nanoparticles fabricated by the auto combustion method, Ceram. Int. 46 (2020) 1–7, https://doi.org/10.1016/j.ceramint.2019.08.074.

[92] K. Chand Verma, Diluted magnetic semiconductor ZnO: magnetic ordering with transition metal and rare earth ions. Magnetic Materials Levitation, IntechOpen, 2021, pp. 1–23, https://doi.org/10.5772/intechopen.90369.